International Journal of Fluid Machinery and Systems
Vol. 8, No. 4, October-December 2015

DOI: 10.5293/IJFMS.2015.8.4.230
ISSN (Online): 1882-9554

Original Paper

Study on Flow Instability and Countermeasure in a Draft tube with Swirling flow

Takahiro Nakashima[1], Ryo Matsuzaka[1], Kazuyoshi Miyagawa[1], Koichi Yonezawa[2] and Yoshinobu Tsujimoto[2]

[1] Department of Applied Mechanics, Waseda University
3-4-1 Okubo, Shinjuku-ku, Tokyo 169-8555, Japan, nakashima@asagi.waseda.jp
[2] Graduate School of Engineering Science, Osaka University
1-3 Fujishirodai, Suita, Osaka 565-8565, Japan

Abstract

The swirling flow in the draft tube of a Francis turbine can cause the flow instability and the cavitation surge and has a larger influence on hydraulic power operating system. In this paper, the cavitating flow with swirling flow in the diffuser was studied by the draft tube component experiment, the model Francis turbine experiment and the numerical simulation. In the component experiment, several types of fluctuations were observed, including the cavitation surge and the vortex rope behaviour by the swirling flow. While the cavitation surge and the vortex rope behaviour were suppressed by the aeration into the diffuser, the loss coefficient in the diffuser increased by the aeration. In the model turbine test the aeration decreased the efficiency of the model turbine by several percent. In the numerical simulation, the cavitating flow was studied using Scale-Adaptive Simulation (SAS) with particular emphasis on understanding the unsteady characteristics of the vortex rope structure. The generation and evolution of the vortex rope structures have been investigated throughout the diffuser using the iso-surface of vapor volume fraction. The pressure fluctuation in the diffuser by numerical simulation confirmed the cavitation surge observed in the experiment. Finally, this pressure fluctuation of the cavitation surge was examined and interpreted by CFD.

Keywords: Draft tube, Cavitation, Hydro turbine, Vortrex rope, Aeration.

1. Introduction

The swirling flow in the draft tube of Francis turbine can cause the flow instability and has a larger influence on hydraulic power operating system. The vortex rope can appear in the draft tube at partial flow rate and can cause lower frequency pressure fluctuation and severe surge problems. According to the recent review by Nishi and Liu [1], those fluctuation may be amplified at a certain cavitation condition and the draft tube cavitation surge occurs. In the past, many research works considered only cavitation coefficient as the primary variable. What has not been given adequate attention is the interaction between fluid turbulence and cavitation. Recently, Ji et al.[2] [3] simulated unsteady cavitating turbulent flow around the twisted hydrofoil based on the Partial-Averaged Navier–Stokes (PANS) approach and discussed the mechanism for the interactions between the cavitation and the turbulent vortices. In addition, their results demonstrated that cavitation promoted the vortex production and the flow unsteadiness. This is an important finding since turbulence is normally attributed to be a factor in the cavitation inception process, but cavitation as a mechanism for turbulent vortex generation and fluid unsteadiness has been given scant attention. These previous researches make us realize the significance of understanding this flow mechanism and the method of suppressing the flow instability. The aeration is known as the main method of the suppression, and it is known that the aeration decreases the efficiency of a water turbine. However, the detail mechanisms of the suppression and the decrease of the efficiency have not been studied sufficiently. Therefore, in present paper, we researched a suppression effect of the aeration and the change of the loss in the diffuser by the aeration using the simple test facility and the model turbine based on our previous work [4] [5]. In addition, we studied the cavitating flow with swirling flow in the diffuser by numerical simulation.

Received January 15 2015; revised July 18 2015; accepted for publication Octoberber 15 2015: Review conducted by Prof. Yoshinobu Tsujimoto. (Paper number O15052S)
Corresponding author: Takahiro Nakashima, nakashima@asagi.waseda.jp

This paper was presented at the 27th IAHR Symposium on Hydraulic Machinery and Systems, September 4, Montreal, Canada.

In order to better resolve the cavitating flow in the draft tube with the swirling flow, the turbulence model is crucial because the cavitation process is basically unsteady in nature and there must be strong interactions between the cavity interface and turbulence. Even though there have been some attempts to predict cavitating flow by using Large Eddy Simulation (LES) [6], very refined mesh and heavy computational resources are needed for prediction. Thus, some hybrid models have been proposed to strike a compromise between RANS and LES. Detached Eddy Simulation (DES) is an attempt to take the best of both by using RANS only in the near wall flow, the attached flow, where the flow is quite stable, and there is a switch from RANS to LES for the detached structures. Recently, Huang et al. [7] has evaluated DES model for cavitation simulation around the 2D hydrofoil and has shown the DES is effective in improving the overall predictive capability of unsteady cavitating flows. However, the result using DES is sensitive to mesh resolution. Another important hybrid model, named Scale-Adaptive Simulation (SAS), was recently proposed by Menter and Egorov [8]. The performance of SAS models in many engineering applications is similar to DES models, but without an explicit influence of the grid spacing on the RANS mode of the model. In the present calculation, we calculated using SAS and a mass transfer cavitation model in order to better resolve the cavitating flow in the draft tube with the swirling flow.

2. Experimental facility

2.1 Draft tube component test facility

Figure 1 shows the framework of the draft tube component test facility. Figure 2 shows the cross-section view of acrylic test section. Degassed tap water was circulated by the centrifugal pump in the experimental facility. The swirling flow generated by the axial swirler flows in the diffuser. Three pressure transducers P_1, P_5, and P_7 are mounted in the axial direction of the diffuser. Other three pressure transducers are mounted in the locations 90°-apart at the same locations. Unsteady pressures and the circumferential phase difference of pressure were measured at these locations. Steady pressures were measured at P_2, P_3, P_4, P_6, P_u, P_d and P_{th}. In addition, the flow in the diffuser was recorded at 500 fps by the high-speed camera. The spread angle of the diffuser is 5.9°. The length of the diffuser is 0.282 m. The cross sectional area ratio between the inlet and the outlet of the diffuser is 5.02.

The flow rate was adjusted by controlling rotational speed of the pump. Besides, the pressures in the diffuser were adjusted by pressurizing or depressurizing the downstream tank. Thus, the experiment covers wide ranges of Reynolds number and cavitation coefficient. In addition, we were able to control the swirl distributions in the diffuser by changing the blade configuration of swirler. In the present tests, the blade outlet angle from axial direction is set to be 70° at the shroud and 80° at the hub. Figure 3 shows velocity distributions at the outlet of the swirler which was analyzed by CFD (ANSYS CFX 14.0). SST k-ω was utilized for turbulence treatment.

First, the experiment was carried out at the flow rate of 650 L/min without the aeration. The flow instability was examined by changing cavitation coefficient. Next, aeration tests were carried out at each typical condition that cavitation surge and vortex rope behaviour occurred. Air was supplied at the downstream locations $0.5D_{th}$-apart from the throat. Two type of aeration tests (natural aeration tests/forced aeration tests) were carried out. In natural aeration tests, air flowed naturally from the atmosphere. In forced aeration tests, air was supplied at four air flow rate (Q_a/Q = 0.25, 0.5, 0.75, 1.0%) by the compressor. In both aeration tests, the loss coefficients was calculated using total pressures at upstream and downstream of the diffuser. Besides, the pressure recovery coefficient was calculated using static pressures of the diffuser throat and the diffuser outlet.

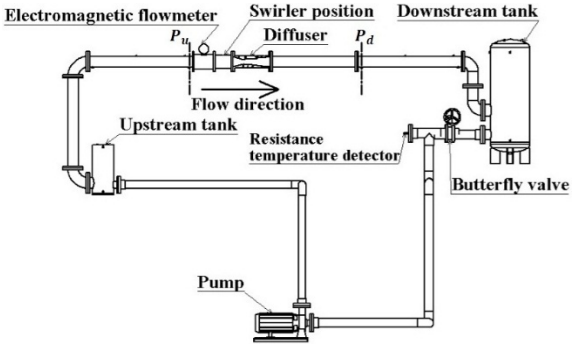

Figure 1. Draft tube component test facility

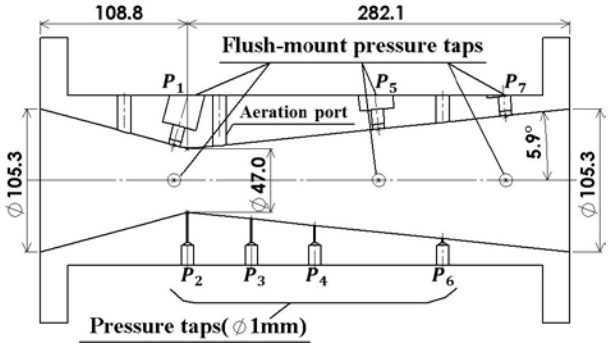

Figure 2. Cross-section view of the diffuser

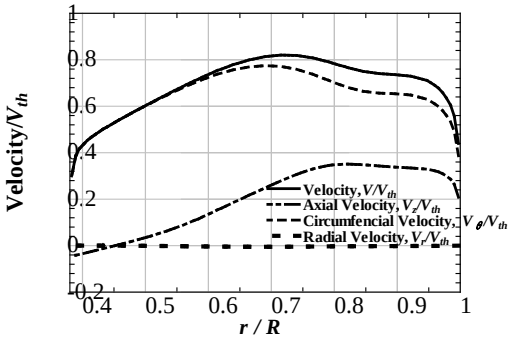

Figure 3. Predicted velocity distributions at the swirler outlet

Table 1. Model turbine specification

Volume Flow	0.056 m^3/s
Effective head	16 m
Rotational speed	900 rpm
Rated power	7.93 kW

2.2 Water turbine test facility

Figure 4 shows the framework of the water turbine test facility. Figure 5 shows the cross-section view of the draft tube. Table 1 shows specification of model water turbine. The spread angle of the diffuser is 5.9°. The length of the diffuser is 0.653 m. The cross section ratio between the inlet and the outlet of the first diffuser and the bend of draft tube is 3.45 and 1.0. Forced aeration (Q_a/Q =0, 0.5, 1.0%) was made at the downstream location 0.5D_{th}-apart from the inlet of the diffuser. Unsteady pressures are measured at P_A, P_B, and P_C.

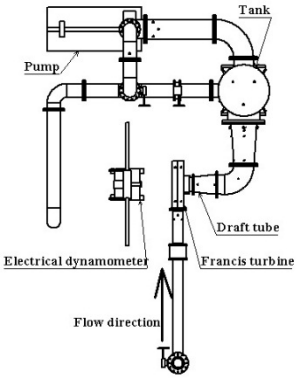

Figure 4. Model turbine test facility

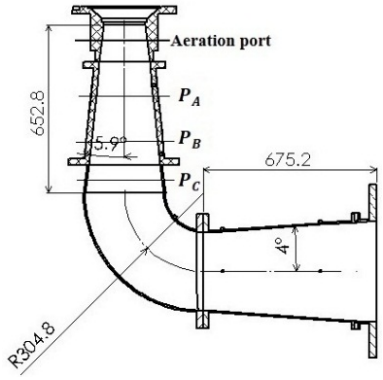

Figure 5. Cross-section view of the draft tube

3. Experimental results and discussion

3.1 Results of Draft Tube component test

Figure 6 shows the spectral analysis of unsteady wall pressures at P_1, P_5 and P_7 at the flow rate of 650 L/min ($R_e = 2.92 \times 10^5$). Figure 7 shows the behaviour of cavitation ($\sigma = 5.12, 4.01$). Through the observation of cavitation, cavitation inception occurred at $\sigma = 7.3$. As shown in Fig. 6, the peak ($S_t = 3.4$), which was observed at only P_1, appears at beyond the range of $\sigma = 4$. The frequency component observed at two points 90°-apart in circumferential direction had phase difference of 90° through cross-spectral analysis. This phase difference suggests that the pressure fluctuation ($S_t = 3.4$) was caused by vortex rope behaviour. Figure 7(a) shows the behaviour of vortex rope. The Strouhal number of vortex rope behaviour was 3.7 evaluated from the pictures, which is corresponding to the spectral analysis ($S_t = 3.4$). Besides, the figure shows that the reason that the frequency component of vortex rope behaviour was not observed at P_5 and P_7 was that the vortex rope did not reach those points. Besides, it should be noted that the amplitude of the pressure at P_1 decreased as the cavitation develops. The main reason for this is that the main flow is choked by cavitation and the change of the effective cross sectional area become lower in this area, which suppresses the occurrence of the vortex breakdown and the vortex rope behaviour in the diffuser.

Next, at all points (P_1, P_5 and P_7), pressure fluctuations ($S_t = 0.23$) which have strong spectral intensity occurred at the cavitation coefficient range of $\sigma = 3 \sim 4$ as shown in Fig. 6. The frequency components have no phase difference in the circumferential direction. In addition, Figure 7(b) shows the volume of cavitation is changing periodically. As a result of calculation of the frequency from the time interval between pictures, Strouhal number is 0.27. Thus, the pressure fluctuation ($S_t = 0.23$) was due to cavitation surge. Moreover, with increase of cavitation coefficient, the Strouhal number of pressure fluctuation changed from 0.8 to 2.0. The reason of this phenomenon could not be identified from the observation of cavity using high-speed camera.

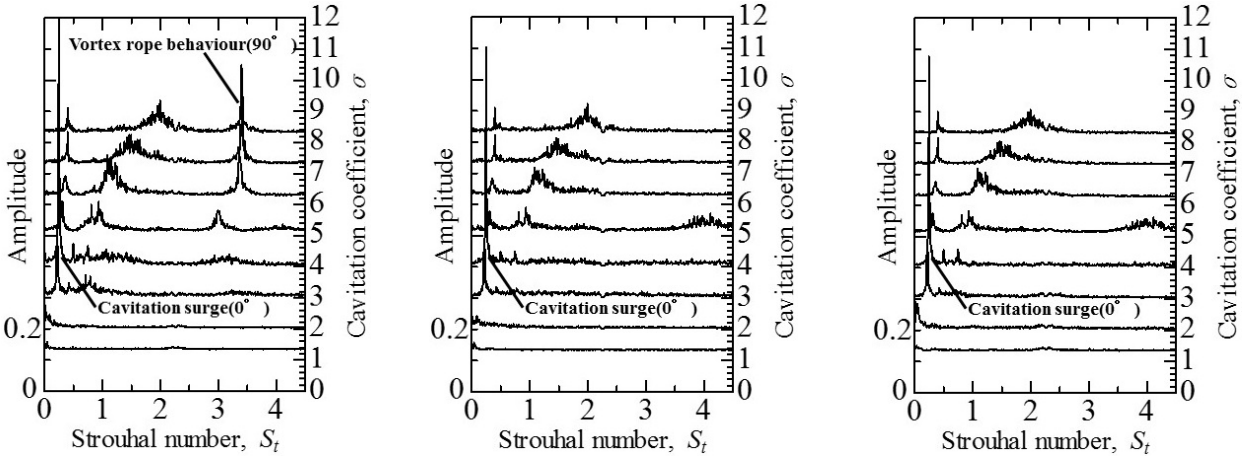

(a) P_1 **(b)** P_5 **(c)** P_7

Figure 6. Frequency domain of pressure fluctuation ($R_e = 2.92 \times 10^5$)

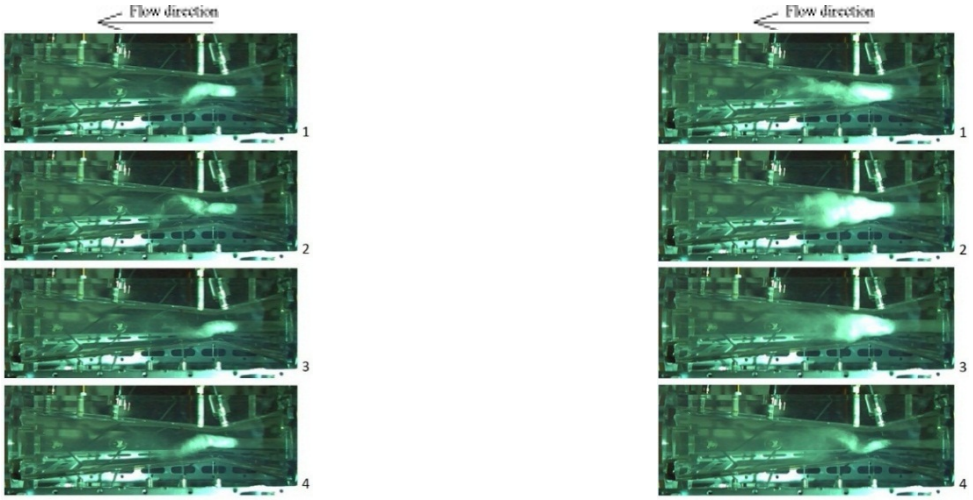

(a) Vortex rope behaviour ($\sigma = 5.12, \Delta t = 0.004\ s$) **(b)** Cavitation surge ($\sigma = 4.01, \Delta t = 0.016\ s$)

Figure 7. Temporal variation of cavitation ($R_e = 2.92 \times 10^5$)

Aeration tests were carried out at typical instability conditions, the flow rate of $Q = 800\mathrm{L/min}$ ($R_e = 3.60 \times 10^5$) and cavitation coefficient of $\sigma = 3.3$ for cavitation surge, and the flow rate of $Q = 650\mathrm{L/min}$ ($R_e = 2.92 \times 10^5$) and cavitation coefficient of $\sigma = 4.8$ for vortex rope behaviour. Figure 8(a) and Figure 8(b) show the spectral analyses of unsteady wall pressures at P_1 when natural aeration tests and forced aeration tests were conducted. In addition, Figure 9 shows the flow in the diffuser for each condition. In natural aeration tests, air flow rate is given as average flow rate, though air flow rate was changing with pressure fluctuation in the diffuser. The flow rate ratios (Q_a/Q) are in Brackets in figures.

Figure 8(a) shows amplitudes of pressure fluctuations caused by cavitation surge are reduced in both aeration tests. Thus, low air flow rate is enough to suppress cavitation surge. Moreover, as shown in Fig. 9(a), passage was filled with air in both aeration tests, which resulted in suppression of cavitation surge.

Next, as shown in Fig. 8(b), the vortex rope behaviour was almost suppressed in natural aeration tests. In addition, the more air made the amplitude of vortex rope behaviour less. Judging from Fig. 9(b), the vortex rope behaviour was still remained in natural aeration tests. Besides, passage was filled with air by forced aeration, which resulted in suppression of vortex rope behaviour as in cavitation surge.

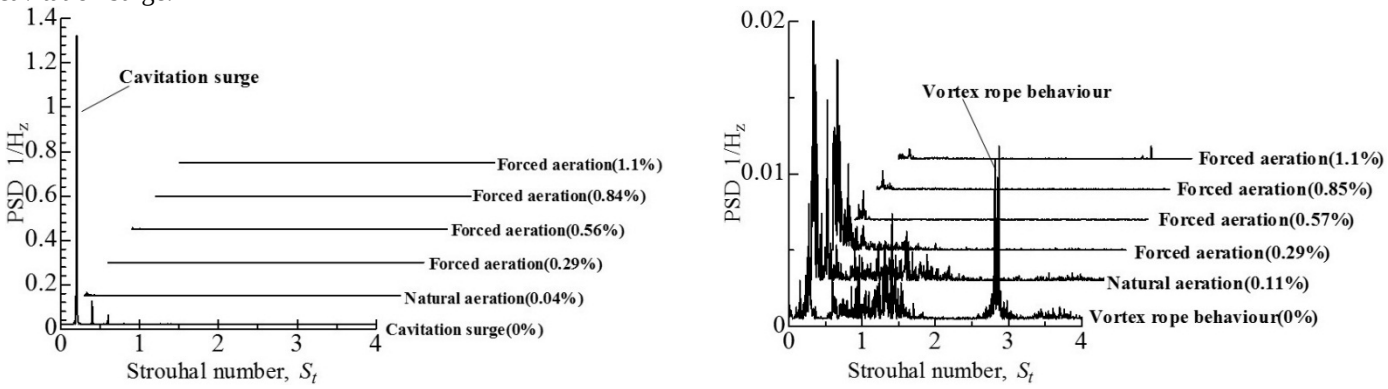

(a) Cavitation surge ($R_e = 3.60 \times 10^5, \sigma = 3.3$) **(b)** Vortex rope behaviour ($R_e = 2.92 \times 10^5, \sigma = 4.8$)

Figure 8. Frequency domain of pressure fluctuation with the aeration

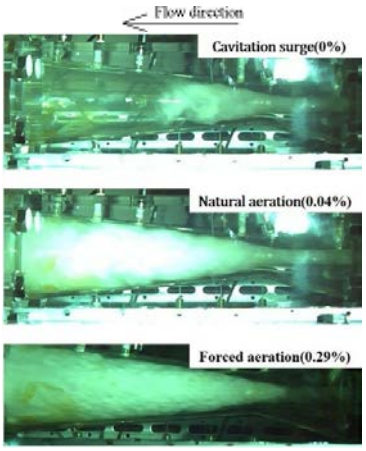

(a) Cavitation surge

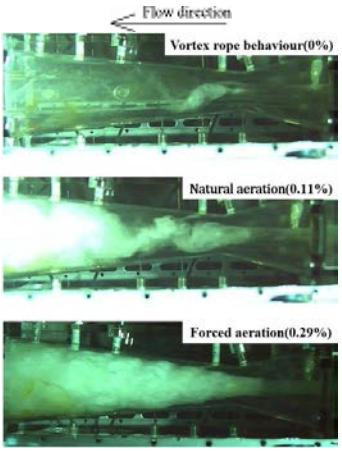

(b) Vortex rope behaviour

Figure 9. Changing the flow in the diffuser by the aeration

The loss coefficient ζ and the pressure recovery coefficient C_p is plotted versus the air flow rate (Q_a/Q) for each typical condition (cavitation surge (a) /vortex rope behaviour (b)) in Fig. 10. The cavitation coefficient of $\sigma = 11.2$, in which cavitation did not occur, was added to the Fig. 10(a), (b). As shown in Fig. 10, the loss coefficient in the diffuser increased with increase of air flow rate. As a result, the loss coefficient became constant, even though the more air was supplied. Pressure recovery coefficient decreased and became negative with increase of air flow rate, resulted from the fact that the pressure loss in the diffuser is larger than the pressure recovery effect.

By comparing two plots at no aeration of Q_a/Q = 0%, the loss in both cavitation conditions (cavitation surge (a) /vortex rope behaviour (b)) was lower than that in no cavitation condition of $\sigma = 11.2$. This shows that cavitation conditions can have an effect of decreasing the loss.

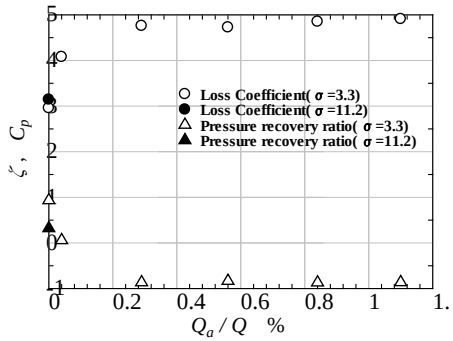

(a) Cavitation surge

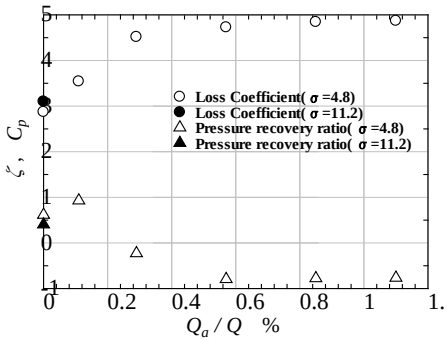

(b) Vortex rope behaviour

Figure 10. Loss Coefficient and pressure recovery coefficient versus the air flow rate

3.2 The results of aeration tests for model water turbine

Figure11 shows the spectral analyses of pressure fluctuation at P_A, P_B, and P_C, in each aeration test using water turbine test facility. With increase of air flow rate, the pressure fluctuation by the vortex rope behaviour was suppressed. And, in the flow rate of Q_a/Q = 1.0 %, there is no pressure fluctuation. In Fig. 12, the amount of decrease of efficiency from the air flow rate of Q_a/Q = 0% is plotted versus air flow rate (Q_a/Q). Thus, the efficiency decreased with increase of air flow rate, the amount of decrease was 3% at the air flow rate of $Q_a/Q = 1.0\%$.

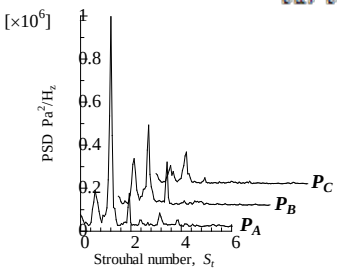

(a) Q_a/Q = 0%

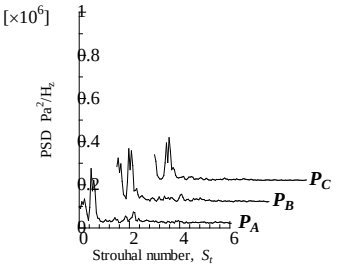

(b) Q_a/Q = 0.5%

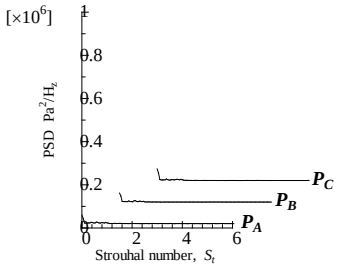

(c) Q_a/Q = 1.0%

Figure 11. Frequency domain of pressure fluctuation in the model turbine test ($R_e = 3.28 \times 10^5, \sigma = 7.9$)

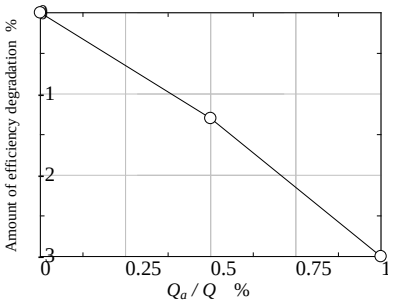

Figure 12. Efficiency degradation by the aeration

4. Numerical method and physical mode

4.1 Governing equations

In this paper, the vapor/liquid two-phase mixture model assumes the fluid to be homogeneous, so the multiphase fluid components are assumed to share the same velocity and pressure. The continuity and momentum equations for the mixture flow are.:

$$\frac{\partial \rho}{\partial t}+\frac{\partial(\rho u_{\mathrm{j}})}{\partial x_{\mathrm{j}}}=0 \tag{1}$$

$$\frac{\partial(\rho u_{\mathrm{i}})}{\partial t}+\frac{\partial(\rho u_{\mathrm{i}} u_{\mathrm{j}})}{\partial x_{\mathrm{j}}}=\rho f_{\mathrm{i}}-\frac{\partial p}{\partial x_{\mathrm{i}}}+\frac{\partial}{\partial x_{\mathrm{j}}}[(\mu+\mu_{\mathrm{t}})(\frac{\partial u_{\mathrm{i}}}{\partial x_{\mathrm{j}}}+\frac{\partial u_{\mathrm{j}}}{\partial x_{\mathrm{i}}}-\frac{2}{3}\frac{\partial u_{\mathrm{k}}}{\partial x_{\mathrm{k}}}\delta_{\mathrm{ij}})] \tag{2}$$

where u_{i} and f_{i} are the velocity and body force in the *i* direction, p is the mixture pressure, μ is the laminar viscosity and μ_{t} is the turbulent viscosity which is closed by the SAS turbulence model. The mixture density, ρ is defined as:

$$\rho=\alpha_{\mathrm{v}}\rho_{\mathrm{v}}+(1-\alpha_{\mathrm{v}})\rho_{\mathrm{l}} \tag{3}$$

where α_{v} is the volume fraction of the vapor component. The subscript v and l refer to the vapor and liquid components.

4.2 Cavitation model

The cavitation model is based on the assumption that the water and vapor mixture in the cavitating flow is a homogeneous fluid. The cavitation process is governed by the mass transfer equation for the conservation of the vapor volume fraction, α_{v}:

$$\frac{\partial(\rho_{\mathrm{v}}\alpha_{\mathrm{v}})}{\partial t}+\frac{\partial(\rho_{\mathrm{v}}\alpha_{\mathrm{v}}u_{\mathrm{j}})}{\partial x_{\mathrm{j}}}=\dot{m}^{+}-\dot{m}^{-} \tag{4}$$

where ρ is the fluid density and u is the flow velocity. The source terms $\dot{m}^{+}$ and $\dot{m}^{-}$ in eq. (4) represent the evaporation and condensation for the phase change during cavitation and the subscript *v* denotes the vapor.

According to the Rayleigh-Plesset equation, the growth of a single vapor bubble depends on the pressure difference between the local static pressure, p, and the saturated vapor pressure, p_{v}. By neglecting the second-order derivative of the bubble radius, which is dominant only during rapid changes in the bubble size, the Rayleigh-Plesset equation can be written as:

$$\frac{dR}{dt}=\sqrt{\frac{2}{3}\frac{|p_{\mathrm{v}}-p|}{\rho_{\mathrm{l}}}} \tag{5}$$

where R is the spherical bubble radius and p is the static pressure. Subscript l denotes the liquid.

The number of bubbles per unit volume, N_{b}, depends on the direction of the phase change. For the initial bubble growth or vaporization period, the main bubble content may be non-condensable gas and N_{b} is calculated from:

$$N_{\mathrm{b}}=(1-\alpha_{\mathrm{v}})\frac{3\alpha_{\mathrm{nuc}}}{4\pi R^{3}} \tag{6}$$

where α_{nuc} is the fraction of non-condensable gas in the liquid.

For the condensation process, the bubbles are almost filled with vapor, so the non-condensable gas fraction in each bubble is neglected. Thus, N_{b} can be determined from:

$$N_{\mathrm{b}}=\frac{3\alpha_{\mathrm{v}}}{4\pi R^{3}} \tag{7}$$

The total mass transfer rate per unit volume is:

$$\dot{m}=N_{\mathrm{b}}\frac{d(\rho_{\mathrm{v}}\cdot 4\pi R^{3}/3)}{dt}=4\pi N_{\mathrm{b}}\rho_{\mathrm{v}}R^{2}\frac{dR}{dt} \tag{8}$$

Combining eqs. (5)~(8), the source terms in Eq. (4) for the vaporization and condensation are given by:

$$\dot{m}^{+}=C_{\mathrm{e}}\frac{3\rho_{\mathrm{v}}(1-\alpha_{\mathrm{v}})\alpha_{\mathrm{nuc}}}{R_{\mathrm{b}}}\sqrt{\frac{2}{3}\frac{\max(p_{\mathrm{v}}-p,0)}{\rho_{\mathrm{l}}}} \tag{9}$$

$$\dot{m}^{-}=C_{\mathrm{c}}\frac{3\rho_{\mathrm{v}}\alpha_{\mathrm{v}}}{R_{\mathrm{b}}}\sqrt{\frac{2}{3}\frac{\max(p-p_{\mathrm{v}},0)}{\rho_{\mathrm{l}}}} \tag{10}$$

where α_{nuc} has the value of 5×10^{-4} for most practical cases. In usual cases, the typical bubble size, R_b, should be 1×10^{-6} m in water. C_e and C_c are empirical coefficients for the vaporization and the condensation processes.

4.3 Numerical algorithm and simulation setup

The unsteady cavitating turbulent flows were simulated using the commercially available CFD package ANSYS-CFX, which is a finite volume code. The time-dependent governing equations were discretized in both the spatial and time domains. The direct coupling method was used to model the cavitating flows in the present calculation. The high order resolution scheme was used for the convection terms with the second-order central difference scheme used for the diffusion terms in the governing equations. The unsteady second order implicit algorithm was used to model the unsteady flow.

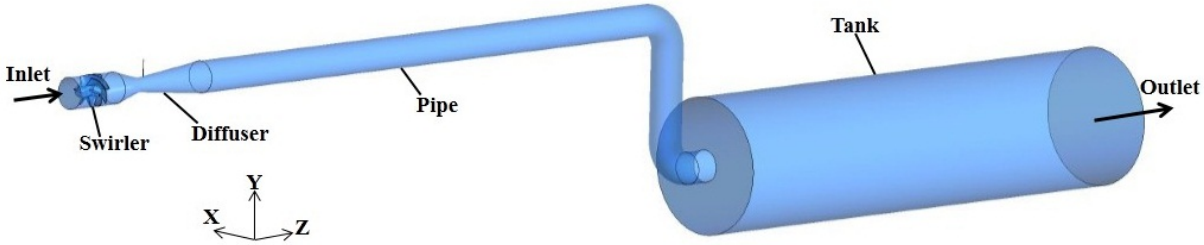

(a) Computational domain and boundary surface

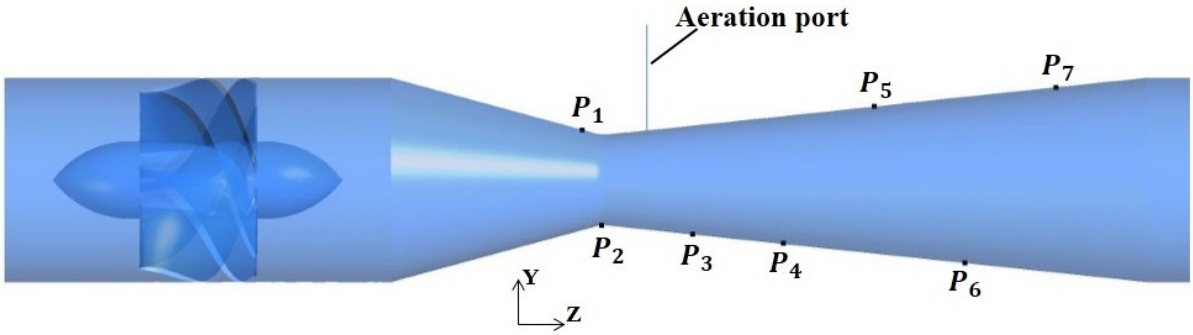

(b) Monitor points along the diffuser surface

Figure 13. Computational domain for the diffuser with swirling flow

The cavitating flow in the diffuser with the swirling flow shown in Fig. 13 was analyzed in present paper. The mesh is composed of approximately 2,500,000 hexahedral elements and 800.000 tetrahedral elements. The boundary conditions are setting as following: inlet flow rates was set to 650 L/min and 800 L/min. The outlet was set as pressure outlet, according to the cavitation coefficient is as follows:

$$\sigma = \frac{P_{out} - P_v}{\frac{1}{2}\rho_l V_{th}^2} \tag{11}$$

where V_{th} is the diffuser throat velocity.

5. Numerical results and discussion

Due to the generation of swirling flow in the swirler, the cavitating vortex rope mainly develops from the head of swirler cone and the cavitation surge may happen in the diffuser. As a result, the vortex rope length or volume is no longer constant and fluctuates dramatically in the diffuser. The combined effect by cavitation and swirling flow in the diffuser caused the very complicated flow phenomenon. According to the present experimental results, there is mainly two type fluctuation occurred in the diffuser. One is caused by the vortex rope behaviour, which happens only at the inlet of diffuser. The other corresponds to cavitation surge and caused by the diffuser effect. First, Figure 14 shows the spectral analysis of pressure at P_1, P_5 and P_7 when the mean flow rate was set at 650 L/min and the cavitation coefficient was changed. These results were compared with the experimental results in Fig. 6. At the condition that cavitation occurred little (σ=6.3), the predicted Strouhal number of the vortex rope behaviour was 3.4 and the measured Strouhal number was 3.4. The result shows that the analytical accuracy of the vortex with almost non cavitating flow is high. In addition, the Strouhal number decreased with a decrease of the cavitation coefficient in the same way as experimental result. However, the vortex rope fluctuation breaks down at $\sigma = 4.0, 5.0$ in experimental result. It is guessed that the reason is because the predicted cavitation volume did not correspond quantitatively to the cavitation volume in experiment. On the other hand, the cavitation surge occurred at only $\sigma = 4.0$ in Fig. 14. This trend corresponds qualitatively to the experimental result.

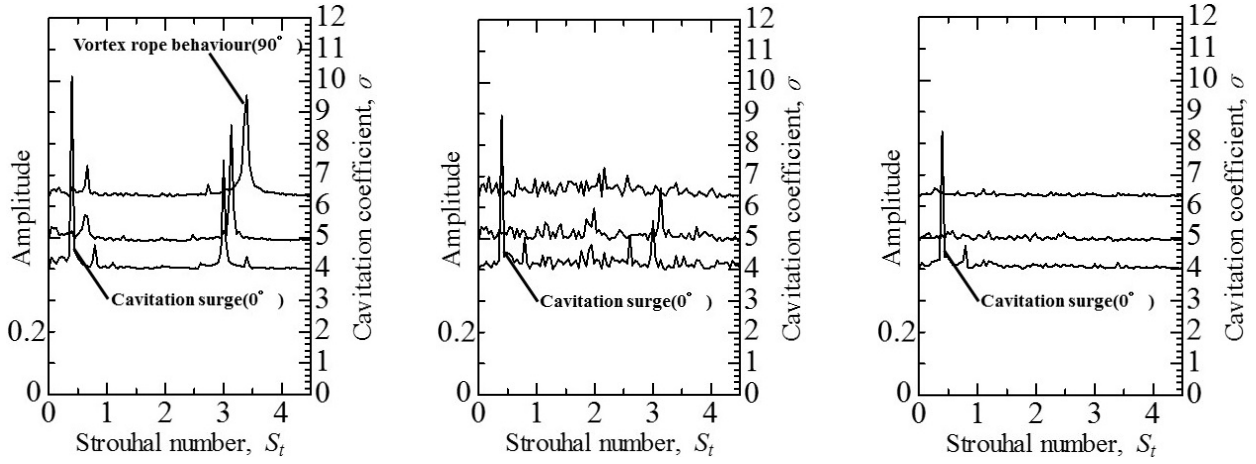

Figure 14. Frequency domain of pressure fluctuation ($R_e = 2.92 \times 10^5$)

In the next place, the analysis was carried out at the flow rate of 800 L/min and the cavitation coefficient of 3.3 to estimate the analysis of the cavitation surge in detail because the cavitation surge occurred particularly clearly at this condition in both of the experiment and the calculation. Figure 15 shows the temporal convergence of the predicted pressure coefficients, K_p, along the different location of the diffuser. The point of $z/D_{th} = 0$ shows the diffuser throat location. The predicted time averaged pressure distribution agrees well with experimental data.

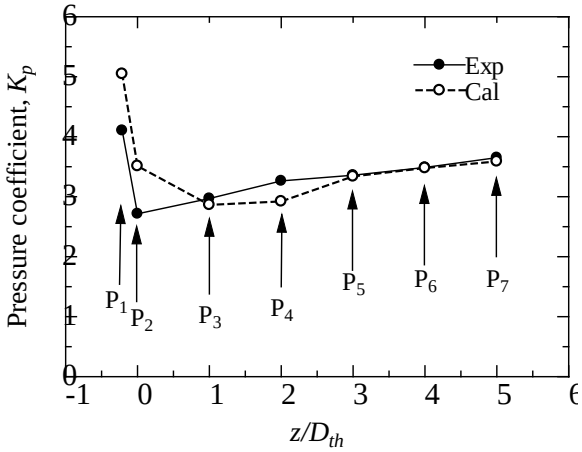

Figure 15. Comparisons of the measured versus predicted pressure coefficients

The evolution of the cavitating vortex flow can be illustrated through the time history of the total vapor volume, V_{cav}, where V_{cav} was defined as:

$$V_{\text{cav}} = \sum_{i=1}^{N} \alpha_i V_i \qquad (12)$$

where N is the total number of control volumes in the computational domain, α_i is the vapor volume fraction in each control volume and V_i is the volume of each cell.

The total vapor volume, V_{cav}, is a convenient parameter for understanding the transient behaviour of cavitating flows in the diffuser. The total vapor volume calculated at each time step is shown in Fig. 16 with snapshots of six typical instants of cavitating vortex rope with iso-surface values of α_v = 0.1 shown in Fig. 17. It should be noted that the choice of the vapor volume fraction value has a direct influence on the cavitation size. A higher value of the vapor volume fraction would result in less difference in terms of cavitation extent, but it tends to hide important details, i.e. interface distortion and cut-off. Based on works by Ji et al [2] [3], we recognize the current selected vapor volume fraction is good to visualize the cavitation mechanisms. Figure 16 indicates that the vapor volume variation due to the cavitation surge in the diffuser is periodic. Figure 18 shows the time history of measured and predicted pressure fluctuation at point P_1, P_5 and P_7 for $\sigma = 3.3$. The predicted pressure frequency was about 9.6 Hz, and the measured pressure frequency was about 5.5 Hz. There were some difference between these frequencies. The reason for this can be that the dynamic characteristic is changed, because the numerical geometry of the passages and the tank is changed from the experimental geometry a little for stabilizing the analysis. In addition, the amplitude of these fluctuation also have a small difference. For comparison, the experimental view pictures are shown at each instant in Fig. 17. For better understandings, the positions of three pressure transducers, named P_1, P_5 and P_7, as well as flow direction are marked in those pictures.

As indicated in Fig. 16 and Fig. 17, the total vapor volume is near the minimum at instant a. In addition, then the vapor volume quickly increased and the tail of the vortex rope developed downstream in the diffuser as shown at instant b, c, d and e in Fig. 17. Meanwhile, it is noted that there is a strong axial adverse pressure gradient appeared in the tail of cavitated vortex rope at instant e, which prevents the cavitated vortex rope to further develop to downstream. After that, the cavitated vortex rope shrinks dramatically and the total vapor volume decreases from instant e to instant f. These complicated processes must be highly related

to dynamic fluctuated pressures in the diffuser. Chen [9] assumed from one dimensional analysis and experimental observation that the diffuser is the cause of this type cavitation surge. There is larger pressure along the axial location of the diffuser and it induces successively an expansion and a contraction of the cavitated vortex rope, which caused the change of total vapor volume in Fig. 16.

Thus, the present simulation reasonably reproduces the cavitation surge behaviour including cavitated vortex rope orbiting in the diffuser and periodical change of the pitch of the helical vortex rope, which agrees qualitatively with experimental observation.

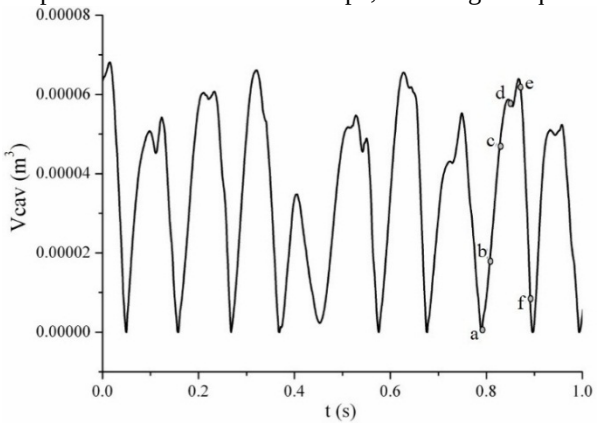

Figure 16. Variation of the cavity volume

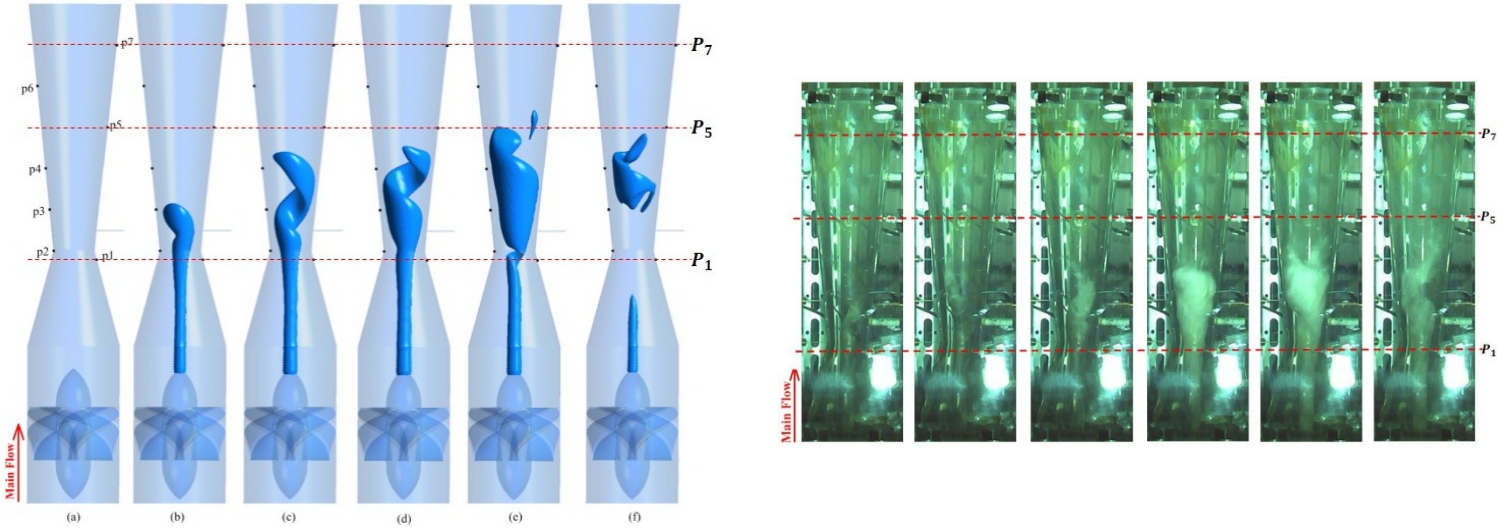

(a) Numerical simulation (time interval 0.02 s) **(b)** Experimental photo (time interval 0.02 s)

Figure 147. Cavitation patterns in the diffuser during one type cycle

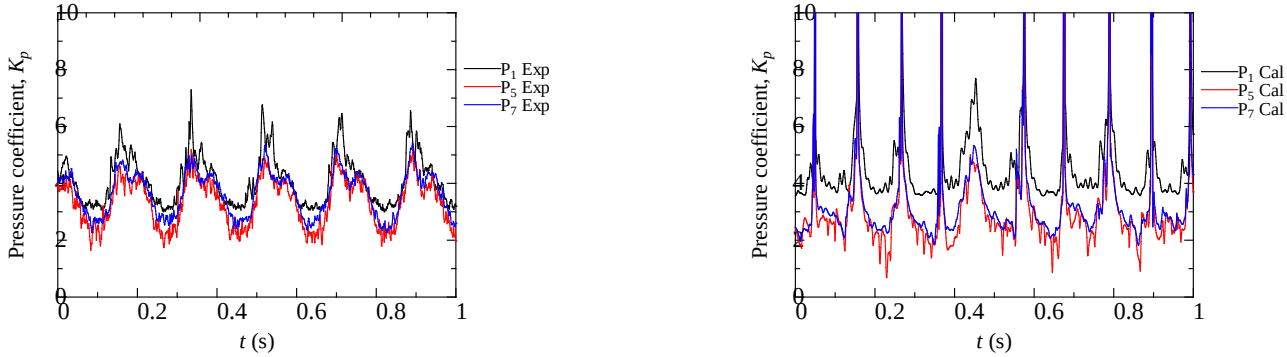

(a) Measured Pressure **(b)** Predicted pressure

Figure 18. Time domain of pressure fluctuation

6. Conclusion

The results obtained from draft tube component test and model turbine test are as follows. In addition, the cavitating flow with swirling flow in the diffuser is studied using Scale-Adaptive Simulation (SAS) with particular emphasis on understanding the unsteady characteristics of the vortex rope structure. Based on the present study, the following conclusions can

be drawn

(1) The pressure fluctuation by the vortex rope behaviour ($S_t = 3.4$) appears in the range $\sigma > 4$ and the pressure fluctuation by the cavitation surge ($S_t = 0.23$) appears at $\sigma = 3 \sim 4$.
(2) The aeration suppress the vortex rope behaviour and the cavitation surge, but the aeration increase the loss in the diffuser and decrease the efficiency of the water turbine by several percent.
(3) The present simulation reasonably reproduces the cavitation surge behaviour including cavitated vortex rope orbiting in the diffuser and periodical change of the pitch of the helical vortex rope, which agrees qualitatively with experimental observation.
(4) A cavitation surge was identified in experiments from the pressure fluctuation in the diffuser. In addition, this pressure fluctuations were examined and interpreted by CFD.

Acknowledgments

The present study was supported by Dr. Luo and Dr. Ji in Tsinghua University. Especially, Dr. Ji gave us valuable suggestions in numerical analysis. The present numerical analysis could be achieved thanks to their advices. We highly appreciate their help.

Nomenclature

l	Diffuser length [m]	ζ	Loss coefficient(=$(P_u + \frac{\rho \bar{u}_u^2}{2} - P_u - \frac{\rho \bar{u}_d^2}{2})/(\rho \bar{u}_{th}^2/2)$)
D_{th}	Diffuser throat diameter [m]	C_p	Pressure recovery coefficient(=$(P_3 - P_{th})/(\rho \bar{u}_{th}^2/2)$)
P_{th}	Diffuser throat pressure [Pa]	R_e	Reynolds number (=$\bar{u}_{th} D/\nu$)
P_v	Saturated vapor pressure [Pa]	σ	Cavitation coefficient (=$(P_{tank} + \rho g h - P_v)/(\rho \bar{u}_{th}^2/2)$)
Q	Flow rate of the main channel [L/min]	S_t	Strouhal number (=$fl/\bar{u}_{th}$)
Q_a	Air flow rate [L/min]	K_p	Pressure coefficient (=$(P - P_v)/(\rho \bar{u}_{th}^2/2)$)
$\bar{u}_{th}$	Diffuser throat average flow velocity [m/s]	f	Frequency [Hz]

References

[1] Nishi, M. and Liu, S. H., 2013, “An Outlook on the Draft-Tube-Surge Study,” International Journal of Fluid Machinery and Systems,” Vol. 6, No. 1, pp. 33-48.
[2] Ji, B., Luo, X. W., Wu, Y. L., Peng, X. X., and Duan, Y. L., 2013, “Numerical analysis of unsteady cavitating turbulent flow and shedding horse-shoe vortex structure around a twisted hydrofoil,” International Journal of Multiphase Flow, Vol. 51, pp. 33-43.
[3] Ji, B., Luo, X. W., Peng, X. X., and Wu, Y. L., 2013, “Three-dimensional large eddy simulation and vorticity analysis of unsteady cavitating flow around a twisted hydrofoil,” Journal of Hydrodynamics, Vol. 25, Issue. 4, p. 510.
[4] Nakashima, T., Matsuzaka, R. and Miyagawa, K., 2014, “Flow instability in the draft tube of the hydro turbine and effects on the efficiency by the suppression,” Proceedings of the Turbomachinery Society of Japan Conference, Japan.
[5] Ji, B., Miyagawa, K., Nakashima, T., Tsujimoto, Y., Yonezawa, K. and Luo, X. W., 2013, “Numerical analysis of cavitation surge in a diffuser with swirling flow,” Proceedings of the Turbomachinery Society of Japan Conference, Japan.
[6] Guo, Y., Kato, C. and Miyagawa, K., 2006, “Large-eddy simulation of non-cavitating and cavitating flows in an elbow draft tube,” 23rd IAHR Symposium, Montreal, Canada.
[7] Huang, B., Wang, G. Y., Yu, Z. Y., and Shi, S. G., 2012, “Detached-eddy Simulation for Time-dependent Turbulent Cavitating Flows,” Chinese Journal of Mechanical Engineering, Vol. 25, Issue. 3, pp. 484-490
[8] Menter, F. R. and Egorov, Y., 2010, “The Scale-Adaptive Simulation Method for Unsteady Turbulent Flow Predictions. Part 1: Theory and Model Description,” Flow Turbul Combust, Vol. 85, Issue. 1, pp. 113-138
[9] Chen, C. K., 2010, “Investigation of Full Load Draft Tube Surge in Hydraulic Power Generating Systerm,” Ph. D. Thesis, Graduate School of Engineering Science, Osaka University, Japan